Authors for correspondence:
Bhargav Rallabandi
e-mail: bhargav@engr.ucr.edu
Howard A. Stone
e-mail: hastone@princeton.edu

Representative subsampling of sedimenting blood

Bhargav Rallabandi[1,2], Janine K. Nunes[2], Antonio Perazzo[2], Sergey Gershtein[3] and Howard A. Stone[2]

[1]Department of Mechanical Engineering, University of California, Riverside, CA 92521, USA
[2]Department of Mechanical and Aerospace Engineering, Princeton University, Princeton, NJ 08544, USA
[3]Abbott Point of Care, Princeton, NJ 08540, USA

BR, 0000-0002-7733-8742; JKN, 0000-0002-1742-2934; AP, 0000-0002-0380-4245

It is often necessary to extract a small amount of a suspension, such as blood, from a larger sample of the same material for the purposes of diagnostics, testing or imaging. A practical challenge is that the cells in blood sediment noticeably on the time scale of a few minutes, making a representative subsampling of the original sample challenging. Guided by experimental data, we develop a Kynch sedimentation model to discuss design considerations that ensure a representative subsampling of blood, from a container of constant cross-sectional area, for the entire range of physiologically relevant hematocrit over a specified time of interest. Additionally, we show that this design may be modified to exploit the sedimentation and perform subsampling to achieve either higher or lower hematocrit relative to that of the original sample. Thus, our method provides a simple tool to either concentrate or dilute small quantities of blood or other sedimenting suspensions.

1. Introduction

Diagnostic assays are an integral part of clinical practice. Whole blood is one of the most common sample types used in diagnostics [1] and is an important material for point-of-care applications as it can be collected relatively easily in small volumes. Blood is made up primarily of blood plasma (about 55% by volume). The remainder is cellular content, the vast majority of which comprises erythrocytes (red blood cells), which outnumber both the slightly larger white blood cells and the smaller platelets that together make up only about

1% of blood volume. Blood plasma comprises about 92% by weight of water with the remaining consisting of dissolved proteins (around 7%), sugars and salts.

The demand for sample analysis at low cost and high accuracy has made microfluidic techniques increasingly popular in recent years. Much attention has been focused on separating plasma from whole blood for diagnostics [2], in particular because traditional centrifugal fractionation of blood can be labour intensive and expensive. Recent studies have sought to address these challenges by developing microfluidic plasma filtration devices using a host of techniques including membrane-based [3,4] or channel-based microfilters [5–7]. Others have used external fields to apply forces to cells and separate them from plasma, including electrokinetic [8], magnetic [9–11], acoustic [12] and inertial [13] forces. Notable within the category of separation devices using external fields are those that exploit the gravitational sedimentation of blood cells [14,15], with some designs additionally making use of fluid flow [16]. Others have developed separation devices on centrifugal microfluidic chips by incorporating microvalves [17] or by employing centrifugal forces in curved or branched microchannels [18]. There has also been an interest in cell-scale processes [19,20], including the effects of erythrocyte morphology and deformability on blood rheology [21,22], and the apparent dependence of blood viscosity on the radius of the capillary (the Fåhræus–Lindqvist effect) [23]. Cell deformability has also been used to develop microfluidic cell sorters [5,24] and plays an important role in the life cycle of erythrocytes [25].

A typical blood sample in diagnostics (extracted, for example, by a pin-prick) has a volume of about 50 µl. By contrast, the volume that can be contained in a microfluidic device is much smaller (typically a few microlitres). Thus, for most diagnostic techniques using microfluidics, it is usually only necessary for a small amount of the original sample to be processed, i.e. the original sample must be 'subsampled' for the diagnostic assay. The cellular constituents of blood are denser than the surrounding plasma and will, therefore, sediment over time due to an external force such as gravity or a centrifugal force. For a typical cell volume fraction—or hematocrit—of about 45%, the sedimentation speeds of erythrocytes under gravity are about $0.2–0.3\,mm\,min^{-1}$. Sedimentation rates are faster for lower cell fractions [15,26,27]. Thus, with processing times on the order of several minutes, sedimentation is appreciable in millimetre-sized geometries: over time, the top of the sample continuously becomes more dilute, while cells aggregate near the bottom of the sample. As discussed above and in previous studies [14,16,28], sedimentation is a useful property for separating plasma from cells. However, demixing of the sample due to sedimentation is counterproductive if the goal is to extract a subsample that is true to the composition of the originally homogeneous sample.

Here, we present experiments and a corresponding model for the sedimentation of erythrocytes in a sample blood volume. Our primary goal is to use the predictions of this model to identify design considerations that allow the extraction of a representative subsample in spite of the continuous sedimentation of the original blood sample. Using experimental measurements, we show that the sedimentation rate of blood as a function of sample hematocrit is well described by a Krieger–Dougherty Law. We then use this sedimentation law to construct a one-dimensional Kynch model that predicts the evolution of cell fraction through space and time. Through the predictions of this model, we identify the region of the design space, which involves the device geometry and the sampling time, for which representative subsampling is possible. Furthermore, we show that the design parameters can be tuned so that the collected subsample achieves a prescribed concentration of cells different from that of the original sample, allowing us to design subsampling protocols to collect either a more dilute or more concentrated extract than the original sample.

The remainder of the paper is organized as follows: §2 introduces the experimental procedure and a model for blood sedimentation that is consistent with these measurements. In this section, we also discuss numerical solutions to the sedimentation model. Then, §3 applies these solutions to the extraction of either representative or non-representative subsamples from the main sample. In §4, we consider the process of subsampling by a microfluidic channel (or network of channels) throughout the sedimentation process and distinguish between pressure-controlled
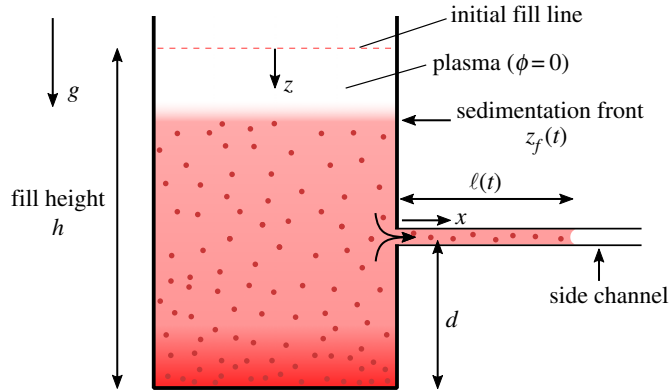
Figure 1. A sketch of the set-up showing a reservoir of cross-sectional area A filled with a blood sample up to a height h (sample volume $\mathcal{V} = Ah$). Connected to the reservoir at a height d is a narrow side channel that continuously draws a small volume of fluid from the reservoir; the fluid collected within the side channel forms the subsample. Over time the suspension in the reservoir sediments and develops a moving front $z = z_f(t)$, such that the reservoir contains only plasma (cell volume fraction $\phi = 0$) between the front and the fill line ($z = 0$). As the sedimentation proceeds, the opening of the side channel is presented with suspension properties that continuously vary in time. An applied horizontal pressure gradient pumps fluid into the side channel, causing it to be filled to a length $\ell(t)$ that increases with time. We seek to optimize the fill height h and placement of the side channel d for optimal subsampling over a specified subsampling time with a prescribed sample hematocrit and volume. (Online version in colour.)

and flux-controlled subsampling protocols. These steps allow us to identify optimal operating and geometric criteria for subsampling of the sedimenting suspension. Conclusions are presented in §5.

2. Sedimentation and design considerations

We are interested in extracting a small volume $\mathcal{V}_s$ of blood from a larger sample of volume $\mathcal{V} > \mathcal{V}_s$. The original sample is homogeneous and has a volume fraction of red blood cells (erythrocytes) $\phi_0 \leq 1$, often referred to as the hematocrit (and expressed as a percentage). The volume fraction is typically around 0.45, though it may be much higher (up to 0.7) or lower (as low as 0.1) depending on physiological or pathological conditions [29]. White blood cells and platelets together make up only about 1% of blood volume and so their contribution to the dynamics discussed below will be neglected.

A typical diagnostic procedure involves filling a reservoir of cross-sectional area A with a known sample volume $\mathcal{V}$ of a suspension such as blood. The fill height is therefore $h = \mathcal{V}/A$. We note that in diagnostics $\mathcal{V}$ is typically specified, whereas A is a design parameter. Connected to the reservoir at a height d from the bottom is a narrow capillary or channel that continuously draws a smaller volume $\mathcal{V}_s$ of the suspension over a sampling time t_s under an applied pressure difference or at a specified flux. Any density mismatch between the suspended cells and the suspending fluid will cause settling of the sample. Thus, the local volume fraction, which we denote as $\phi(\mathbf{x}, t)$, evolves in both space $\mathbf{x}$ and time t. Assuming no loss of liquid on time scales of interest (for example, to evaporation) the volume fraction satisfies $(1/\mathcal{V}) \int_\mathcal{V} \phi(\mathbf{x}, t) \, d\mathcal{V} = \phi_0$, where the integral is over the entire sample volume, including the volume drawn into the side channel (figure 1).

Our objective is to identify geometric parameters of the main reservoir and the side channel (involving A, $\mathcal{V}$ and d) that ensures a representative subsampling in the side channel over a desired time t_s, given an initially homogeneous suspension with volume fraction ϕ_0 that settles over time. Here, we further focus on blood and ask whether it is possible to identify a single design that can be used for the entire range of physiologically relevant hematocrit ($0 < \phi_0 \lesssim 0.75$).

We assume that the side channel draws a sufficiently small volume of suspension so that the sedimentation in the main channel and the extraction (subsampling) by the side channel can be considered separately. We first consider, using experiments and modelling, the sedimentation of blood in the reservoir.

(a) Sedimentation experiments

We characterize the sedimentation of blood in a reservoir similar to that sketched in figure 1, but in the absence of a side channel. In a chamber of constant cross section, the sedimentation is quasi-one-dimensional and can be quantified experimentally by front-tracking, as we describe below. The sedimentation velocity v of erythrocytes depends on several factors including the mean hematocrit [30], the protein content of the plasma [31], the age of the sample, pathological and physiological conditions, and the presence of additives [29]. Here, we focus on the dependence of v on ϕ, which is particularly important as the local hematocrit of a given sample of blood changes during the sedimentation process. Despite the many variables controlling the sedimentation rate, it is agreed that the sedimentation rate decreases with hematocrit, provided the geometry is large compared with the size of the cell and cell-aggregates [32].

We quantify the dependence of sedimentation rate on hematocrit by direct measurements. Unspun whole blood with tri-potassium ethylenediaminetetraacetic acid (EDTA, an anti-coagulant) was received from the Biological Specialty Corporation (Colmar, PA). The blood was centrifuged at 3000 r.p.m. for 10 min to separate the red blood cells from the plasma; the blood, as received, was 45% hematocrit. Then, 10 ml each of different hematocrit samples were prepared by mixing different volume ratios of cells and plasma in 15 ml centrifuge tubes (inner diameter = 1.4 cm). Prior to sedimentation, the tubes were inverted repeatedly and gently by hand to mix the suspensions, and then placed upright in Styrofoam racks. Images were captured every minute during sedimentation (Nikon D5100, Camera Control Pro). The images were analysed using ImageJ software [33] to track the location of the sedimentation front over time $z_f(t)$ (figure 1). Consistent with previous studies [15,30,32], we observe that the sedimentation front moves at a roughly constant speed over a range of times. We determine the maximum sedimentation rate for each hematocrit by analysing this part of the displacement versus time curve (see [30]). Over this time range, the suspension has not changed significantly in composition, and therefore the measured sedimentation rate can be considered a function of the mean sample hematocrit ϕ_0, which approximates the local hematocrit ϕ, i.e. $v = v(\phi) = \mathrm{d}z_f/\mathrm{d}t$. We will show that this approximation is self-consistent in subsequent sections.

Sedimentation experiments were conducted simultaneously in four tubes per hematocrit at room temperature (21–22°C). Figure 2a plots the sedimentation speed as a function of the sample hematocrit, extracted from our measurements (solid circles), alongside the measurements of Rourke & Ernstene [30] (triangles). In both cases, we find that the data are well fit by a sedimentation law of the form

$$v(\phi) = v_0 \left(1 - \frac{\phi}{\phi_m} \right)^k , \qquad (2.1)$$

where v_0 is the sedimentation speed in the dilute limit, ϕ_m is the hematocrit at which no sedimentation can be observed and k is a dimensionless exponent. With $\phi_m = 0.75$, a best fit to our data gives $v_0 \approx 1.76 \, \mathrm{mm \, min^{-1}}$ and the exponent $k \approx 2.75$, while a fit to the data of [30] yields $v_0 \approx 3.81 \, \mathrm{mm \, min^{-1}}$ and $k \approx 3.03$.

Equation (2.1) may also interpreted in terms of a Krieger–Dougherty Law [34] for the viscosity of a suspension $\eta(\phi) = \eta_0(1 - \phi/\phi_m)^{-k}$ by writing $v(\phi) = g(\Delta m)/6\pi a \eta(\phi)$, where a is a length-scale characterizing Stokes drag on an erythrocyte, Δm is its buoyant mass, g is the gravitational acceleration and η_0 is the plasma viscosity. We recognize that this description is only approximate since blood is a complex fluid that is shear-thinning, slightly viscoelastic and has a small yield stress (1–10 mPa) [35]. However, its rheology is often well described by a Casson Law [36,37], which, in the limit of a small yield stress, reduces to a Newtonian effective-viscosity description such as the one used above.
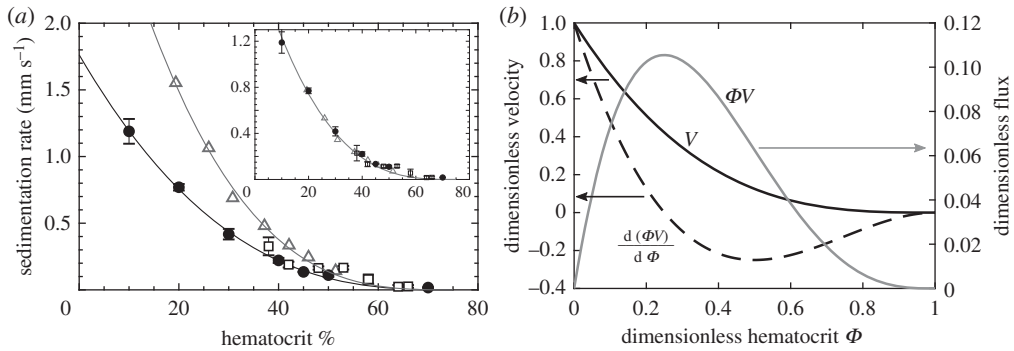
Figure 2. (*a*) Experimentally measured sedimentation rates as a function of the hematocrit: filled circles and open squares indicate two sets of present experimental results (whole blood samples from two different anonymous donors) and triangles are the data of [30]. Error bars indicate one standard deviation. Curves are best fits of the sedimentation law (2.1) with $\phi_m = 0.75$; a fit to the current experiments (circles) yields $v_0 \approx 1.76$ mm min^{-1}, $k \approx 2.75$ and the fit to the data of [30] results in $v_0 \approx 3.81$ mm min^{-1}, $k \approx 3.03$. The inset plots the same data but with the sedimentation rates represented by squares and triangles being scaled by uniform factors of 0.7 and 0.5, respectively, showing that all three datasets are similar up to scale. (*b*) Dimensionless sedimentation velocity $V(\Phi) = (1 - \Phi)^k$ (solid; left axis), flux $J(\Phi) = \Phi V$ (solid; right axis) and wave speed $U(\Phi) = d(\Phi V)/d\Phi$ (solid; left axis) with $k = 3$. The flux is maximum when $\Phi = (1 + k)^{-1}$.

To further validate our data, we performed separate measurements with a different whole blood sample (obtained from a different anonymous donor) of volume $\approx 60\,\mu$l in a narrow capillary tube (inner diameter of 1.1–1.2 mm). Sedimentation rates were measured using a similar procedure as the one described above. The results of these measurements are indicated as open squares in figure 2*a* and are largely consistent with the data obtained in the wider tubes (circles). Both datasets corresponding to the present experiments suggest slower sedimentation compared with [30], which we speculate may be due to factors such as differing physiological or pathological conditions that we do not control (cf. [32]). Interestingly, within the range of measurement, the datasets differ by a scale factor between 0.5 and 0.7 but are nearly identical in shape, as indicated in the inset of figure 2*a*. As noted above, the detailed values of v_0 and k may depend on factors other than the hematocrit and are not central to the discussion below. The key feature is that the Krieger–Doughery-like sedimentation law (2.1) provides a good representation of the dependence of sedimentation speed on the hematocrit of the sample. This finding will be used to construct the sedimentation model discussed next.

(b) Sedimentation model

We model the settling of the suspension using a one-dimensional Kynch model [38,39], where the sedimentation speed depends only on the local volume fraction of cells, which in turn evolves in space and time. We assume that the properties of the suspension vary only along the direction of gravity and so write $\phi = \phi(z, t)$, taking $z = 0$ to represent the top of the initial sample and $z = h$ to be the bottom of the reservoir (figure 1). Then, conservation of cell number in the reservoir containing the original sample can be expressed as

$$\frac{\partial \phi}{\partial t} + \frac{\partial(\phi v(\phi))}{\partial z} = 0. \tag{2.2}$$

Note that we have neglected the loss of cells (and plasma) into the subsampling side channels, which implicitly assumes that the subsample volume is much smaller than that of the original sample ($\mathcal{V}_s \ll \mathcal{V}$), as discussed previously. We also assume that the side channel is sufficiently narrow to be able to sample the properties of the suspension at a single height d from the bottom (cf. figure 1), and that the flow into the side channel does not influence the sedimentation in the

main container. This loss of sample into the side channel may be modelled within the present framework by a point sink of material placed at a distance $z = h - d$ (coupling the sedimentation in the reservoir with the flow through the side channel), though we will neglect it in our discussion below and consider a one-way coupling only (see §3).

For a one-dimensional model, the physically relevant boundary condition is that of zero cell flux $\phi v(\phi)$ at the top and bottom boundaries. We also assume that the reservoir is instantaneously filled with a spatially uniform sample, $\phi(0 < z < h, t = 0) = \phi_0$.

Introducing dimensionless variables $Z = z/h$, $T = t v_0 / h$, $\Phi = \phi / \phi_m$ and defining

$$V(\Phi) = \frac{v(\phi)}{v_0} = (1 - \Phi)^k, \tag{2.3}$$

sedimentation in the reservoir is governed by

$$\frac{\partial \Phi}{\partial T} + \frac{\partial (\Phi V(\Phi))}{\partial Z} = 0 \quad \text{with} \tag{2.4a}$$

$$\Phi V(\Phi) = 0 \quad \text{at } Z = 0 \text{ and } Z = 1 \tag{2.4b}$$

and

$$\Phi(Z, T = 0) = \Phi_0 \equiv \frac{\phi_0}{\phi_m} \le 1. \tag{2.4c}$$

The sedimentation flux $J(\Phi) \equiv \Phi V(\Phi)$ is zero both when $\Phi = 0$ and $\Phi = 1$. Because the problem is hyperbolic, it is useful to define a wave speed [40]

$$U(\Phi) = \frac{\mathrm{d}J(\Phi)}{\mathrm{d}\Phi} = (1 - (1 + k)\Phi)(1 - \Phi)^{k-1}, \tag{2.5}$$

which is positive for $\Phi < 1/(1 + k)$ and negative for $\Phi > 1/(1 + k)$ (figure 2b). We note that it is appropriate to pose the problem with two boundary conditions in Z despite (2.4a) being first order in Z since the problem is hyperbolic and information may propagate into the domain at either boundary depending on the sign of U [40]. In figure 2b, we plot $V(\Phi)$, $J(\Phi)$ and $U(\Phi)$ according to the sedimentation model (2.3), with $k = 3$. The side channel, which is located at the dimensionless distance $D = d/h$ from the base of the reservoir, continuously samples the fluid at $Z = 1 - D$, and thus may encounter a range of suspension properties over an interval of time. It is useful to define the time-averaged hematocrit $\overline{\Phi}$ at a location Z during a time interval T by

$$\overline{\Phi}(Z, T) \equiv \frac{1}{T} \int_0^T \Phi(Z, T') \, \mathrm{d}T', \tag{2.6}$$

which is a useful measure of the average properties encountered at the entrance of the side channel, with $Z = 1 - D$. We note that the characteristic velocity v_0 corresponds to the dilute ($\phi_0 \to 0$) limit and is typically an order of magnitude greater than the sedimentation rate of typical blood ($\phi_0 \approx 0.45$); see figure 2a.

(c) Numerical solutions

We solve the hyperbolic problem defined by equations (2.4a–c) using a first-order conservative Godunov-type scheme with upwind differencing in the direction of the local wavespeed U [41]. Here and below, we use $k = 3$, consistent with experimental data (figure 2). Instantaneous and time-averaged concentration profiles obtained from a typical simulation with an initially uniform concentration Φ_0 are plotted in figure 3a,b, respectively. As is typical of sedimenting suspensions, the system evolves by the formation of a front with position $Z = Z_f(T)$ that propagates towards the bottom of the container (the positive Z direction). Upstream of the front, the suspension contains only fluid ($\Phi = 0$) while downstream of the front the concentration of the suspension is either greater than or equal to its initial value Φ_0. Additionally, a compression wave propagates rearward (towards $Z = 0$) from the no-flux boundary at $Z = 1$ (the base of the reservoir), as shown in figure 3. The concentration increases behind this compression wave (as measured in its direction of propagation), corresponding to cells settling at the bottom of the container. Between
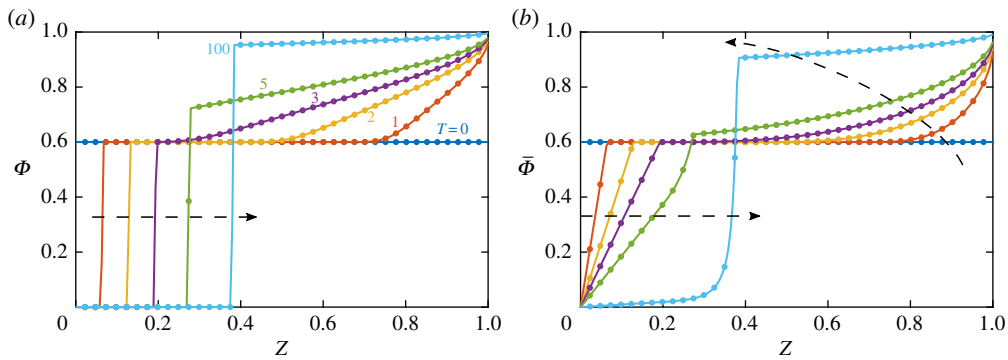
Figure 3. Results of a typical simulation with initial condition $\Phi(Z, T = 0) = \Phi_0 = 0.6$ ($\phi_0 = 0.45$, $\phi_m = 0.75$, $k = 3$; typical for blood) showing profiles of (a) the instantaneous hematocrit $\Phi(Z, T)$ and (b) the mean hematocrit $\overline{\Phi}(Z, T)$ as functions of the spatial coordinate Z, at times $T = \{0, 1, 2, 3, 5, 100\}$. Dashed arrows indicate profiles at increasing T. A sedimentation front propagates towards $Z = 1$ (the base), while a compression wave propagates towards $Z = 0$, until the two meet. (Online version in colour.)

the forward travelling sedimentation front and the rearward propagating compression wave is a 'quiet' region where $\Phi = \Phi_0$. This region shrinks and eventually vanishes as the two waves meet (around $T = 3$ in figure 3). This process determines the largest time for which the subsample is representative of the original sample, which we discuss in detail in §3.

The speed of the sedimentation front is given by the Rankine–Hugoniot condition

$$\frac{\mathrm{d}Z_f}{\mathrm{d}T} = \frac{[J]_{Z_f}}{[\Phi]_{Z_f}}, \tag{2.7}$$

where $[f]_Z = f|_{Z^+} - f_{Z^-}$ is the jump of a quantity f around the point Z. We note that in an unconfined system, or at sufficiently short times, $\Phi(Z > Z_f) = \Phi_0$ and $\Phi(Z < Z_f) = 0$, so that $\mathrm{d}Z_f/\mathrm{d}T = V(\Phi_0)$. Thus, the identification of the experimentally measured front speed $\mathrm{d}z_f/\mathrm{d}t$ (in a range where the front speed is constant over time) with the sedimentation rate $v(\phi)$ in a Kynch model is self-consistent, as indicated in §2a. Under vertical confinement, the system eventually reaches a static final state. Mass conservation dictates that the sedimentation front approaches a fixed position $Z_f \to 1 - \Phi_0$ as $T \to \infty$, so that $\Phi(Z, T \to \infty) = \Theta[Z - (1 - \Phi_0)]$, where Θ is the Heaviside step function (figure 3).

3. Subsampling the sedimenting suspension

Solutions of equation (2.4) may be analysed further using the method of characteristics though this is not the primary focus of the present work. An overview of contributions to Kynch sedimentation as well as solution techniques, including the method of characteristics, are detailed in [39]. Here, we are interested in sampling the sedimenting suspension—whose properties evolve in both space and time—in a way that is predictable and therefore of potential value to diagnostics. For applications, it is often necessary that the side channel subsamples the sedimentation suspension for a prescribed sampling time t_s, which defines a sampling window $T \in [0, T_s \equiv t_s v_0/h]$. Typically, t_s is set by the application and v_0 is a property of the suspension, with h being a design parameter. Thus, we have three dimensionless parameters: the hematocrit of the sample Φ_0, the sampling time T_s (related to the fill height), and the location of the subsampling port $D = d/h$; Φ_0 is an input while T_s and D are design parameters.

We are interested in finding the region of the design space (T_s, D) for which the side channel samples a target hematocrit to within a specified tolerance. We introduce two variants of this problem:

8

royalsocietypublishing.org/journal/rspa   *Proc. R. Soc. A* **475**: 20190223

(i) the side channel instantaneously samples only the original sample hematocrit throughout the sampling time window, i.e. $\Phi(1 - D, 0 < T < T_s) = \Phi_0$, and

(ii) the side channel samples a target mean hematocrit Φ^* (generally $\neq \Phi_0$) over the sampling window, i.e. $\overline{\Phi}(1 - D, T_s) = \Phi^*$.

In both cases, we may specify a physical tolerance $\delta\Phi$ up to which the equalities in statements (i) or (ii) above must hold. Note that a solution to (i) automatically solves (ii) if $\Phi^* = \Phi_0$. Due to the finite 'quiet' region downstream of the sedimentation front as discussed above (cf. figure 3), solutions to problem (i) generally result in finite regions in the (T_s, D) design space even for arbitrary small tolerance. By contrast, a solution of (ii) seeking a target mean concentration $\overline{\Phi}(1 - D, T_s) = \Phi^* \neq \Phi_0$ will result in solution regions whose 'size' scales with the tolerance $\delta\Phi$.

(a) Representative subsampling

We first consider the case where we demand that the subsample collected in the side channel is representative of the original sample hematocrit Φ_0 throughout the sampling interval $0 < T < T_s$, corresponding to problem (i) introduced above. Thus, for a specified Φ_0, we solve the system (2.4) to obtain $\Phi(Z, T)$ and then identify combinations of sampling times $T = T_s$ and side channel locations $Z = 1 - D$ for which

$$\Phi_0 - \delta\Phi \leq \Phi(1 - D, T_s) \leq \Phi_0 + \delta\Phi. \tag{3.1}$$

As noted above we may in principle obtain solution regions with finite size in phase space for $\delta\Phi = 0$, although doing so numerically is non-trivial. For the results below, we use a small tolerance of $\delta\Phi = 10^{-3}$ to accommodate numerical errors.

Admissible solutions (T_s, D) of (2.4) and (3.1) are indicated as shaded regions in figure 4 for different values of Φ_0. These solution regions in the phase plane are of roughly triangular shape with details that depend on Φ_0. In the limit of arbitrarily short sampling times, the concentration at any location D is identical to the initial concentration Φ_0, thus identifying one of the solution boundaries with the $T_s = 0$ axis. Furthermore, we observe that $\Phi = \Phi_0$ just downstream of the sedimentation front for short times (figure 3) identifying another boundary of the triangular solution region with the trajectory of the front, $Z = V(\Phi_0)T$ or $D = 1 - V(\Phi_0)T$. The third side is set by the speed of the backward propagating compression wave (cf. figure 2b) that starts at $Z = 1$ ($D = 0$), although this speed of propagation is not trivial to obtain as a function of Φ_0.

As figure 4 shows, solution regions (T_s, D) depend strongly on the initial hematocrit Φ_0. However, it may be important in an application to obtain a representative subsample of the original suspension over a range of initial concentrations Φ_0. Designing such an application that is viable for any value Φ_0 therefore requires us to identify the region of intersection of solutions over the entire range of $\Phi_0 \in (0, 1)$. We estimate the size of this intersection region by considering the fastest sedimenting front and the fastest (rearward moving) compression wave. The fastest sedimentation wave travels with a velocity $V_{max} = \max_{\Phi_0}\{V(\Phi_0)\} = 1$ corresponding to a trajectory $Z = T$ (or $D = 1 - T_s$; figure 4). The fastest rearward propagating waves are determined by the fastest negative wavespeeds in the system (cf. figure 2b). The maximum negative wavespeed is $U_{max}^- = U(\Phi_{max}^-) < 0$ where Φ_{max}^- is identified by $dU(\Phi)/d\Phi = 0$; for example, $\Phi_{max}^- = \frac{1}{2}$ and $U_{max}^- = -\frac{1}{4}$ for $k = 3$. Thus, backward propagating waves are bounded by the trajectory $Z = 1 + U_{max}^- T$ (or $D = -U_{max}^- T_s$; figure 4). These limiting forward and backward waves intersect at $T_s = T_s^c = (1 - U_{max}^-)^{-1}$ and $D = D^c = 1 - T_s^c$. Thus, representative subsampling is guaranteed for any Φ_0 within the triangular design-space region defined by the points

$$(T_s, D) = \left\{(0, 0); \quad (0, 1); \quad \left(T_s^c = \frac{1}{1 - U_{max}^-}, D^c = \frac{-U_{max}^-}{1 - U_{max}^-}\right)\right\}, \tag{3.2}$$

where we recall that $U_{max}^- \leq 0$ and therefore both D^c and T_s^c are smaller than unity. This region is hatched in figure 4, showing good agreement with numerical results. Thus, placing the side
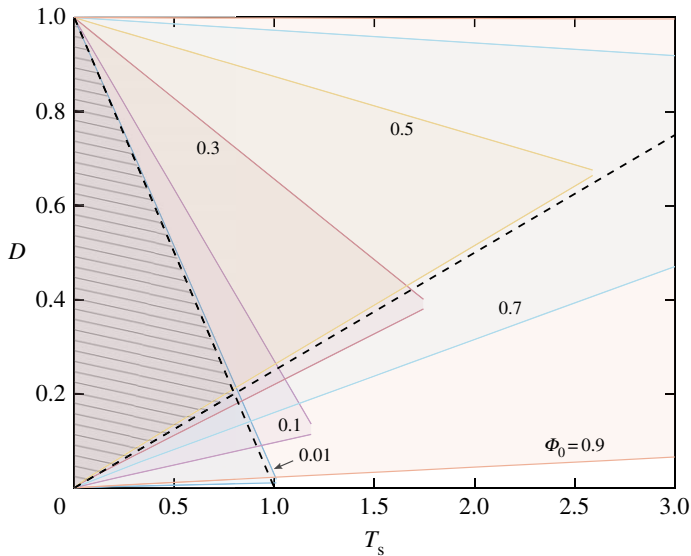
Figure 4. Combinations of the dimensionless side channel height D and the dimensionless sampling time T_s, using $k = 3$ in (2.3), for which the subsample is representative of the original sample, indicated as shaded regions for different values of Φ_0, with a tolerance $\delta\Phi = 0.001$. The subsample is not representative of the original sample outside the shaded region for a particular Φ_0. The regions are roughly triangular in shape. Dashed lines indicate the fastest forward and rearward propagating waves, which intersect at the point ($T_s = 4/5$, $D = 1/5$). Along with the $T_s = 0$ axis, this point defines the triangular region of the design space (hatched) that ensures a representative subsampling for any hematocrit Φ_0 (see equation (3.2)). (Online version in colour.)

channel at height $D = D^c$ allows the largest sampling time $T_s = T_s^c$ for any Φ_0; for $k = 3$, $T_s = T_s^c = 4/5$ and $D = D^c = 1/5$.

We note that in practice the physical sampling time t_s and the range of hematocrit is often prescribed so it may be necessary to choose h, or equivalently the dimensionless quantity $T_s = t_s v_0/h$, as a design parameter. A slightly different but equivalent visualization of figure 4 is shown in figure 5, where the permissible range of D is plotted against Φ_0 as shaded regions for different values of T_s. For small T_s, the range of allowable D for representative sampling is finite across the entire range of Φ_0 values (e.g. $T_s \leq 0.6$ in figure 5). As T_s increases up to a critical value, the range of allowable D decreases to a point: at $T_s = 0.8$, only a single choice of $D \approx 0.21$ (dotted line) can guarantee a representative subsampling over all Φ_0 values, consistent with the theoretical predictions $D = D^c$, $T_s = T_s^c$ in (3.2). For larger sampling times $T_s^c < T_s \leq 1$, no single value of D is suitable for all Φ_0 although individual solutions $D(\Phi_0)$ exist for any choice of Φ_0. For even larger sampling times $T_s > 1$, representative subsampling is only possible for sufficiently large hematocrit (sufficiently slow sedimentation), as indicated by the solution for $T_s = 1.5$ in figure 5; for example, no representative subsampling solutions $D(\Phi_0; T_s = 1.5)$ exist for $\Phi_0 \lesssim 0.2$.

(b) Oversampling and undersampling

As we have shown above it is possible to obtain a representative subsample of the original sample, but only within a finite region of the dimensionless design space (T_s, D). Outside of this solution region, the collected subsample will on average differ in hematocrit from that of the original sample Φ_0. This feature presents the possibility of developing a design that is capable of controlled undersampling ($\overline{\Phi}(Z, T) < \Phi_0$) or oversampling ($\overline{\Phi}(Z, T) > \Phi_0$) the suspension on average in a systematic way. Such a design may be useful to extract a more dilute or concentrated version of the original sample without the need for an extra separation or mixing step.
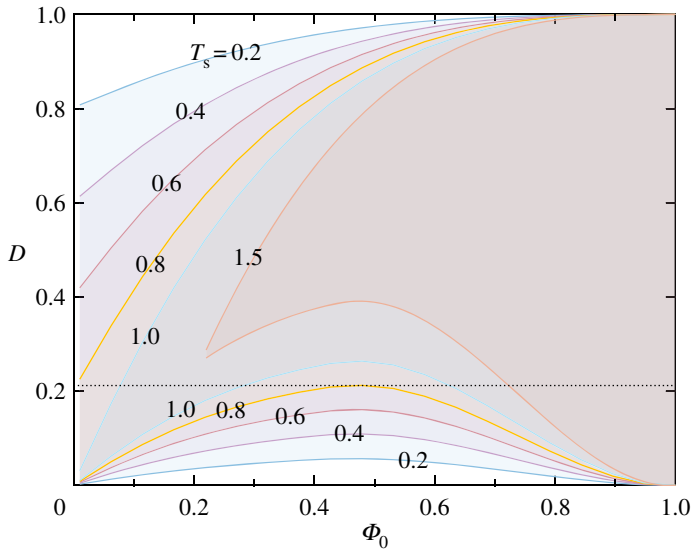
Figure 5. Map of the permissible range of D and sample hematocrit Φ_0 for representative sampling (tolerance $\delta\Phi = 0.001$), indicated as shaded regions for different sampling times T_s, using $k = 3$ in (2.3). The subsample is not representative of the original sample outside the shaded regions for a prescribed T_s. The data here are equivalent to those of figure 4. The dotted horizontal line represents the limiting value $D \approx 0.2$ that is marginally within the solution space for all Φ_0 and occurs for $T_s \approx 0.8$, in agreement with the prediction of equation (3.2). (Online version in colour.)

We denote the target mean hematocrit of the subsample by Φ^*, so that we seek to design a subsampling protocol that achieves

$$\Phi^* - \delta\Phi \leq \overline{\Phi}(1 - D, T_s) \leq \Phi^* + \delta\Phi. \tag{3.3}$$

Of particular interest are cases where $\Phi^* \neq \Phi_0$ since for $\Phi^* = \Phi_0$ (up to $\pm\delta\Phi$) the solution to this problem is similar to that of §3a. For the inverse problem posed here, $\delta\Phi$ is a physical design tolerance on the desired concentration of the subsample. Numerical errors are necessarily much smaller than $\delta\Phi$.

As discussed earlier in §3, the size of the solution region for $\Phi^* \neq \Phi_0$ will strongly depend on both Φ^* and the tolerance $\delta\Phi$, and will vanish as $\delta\Phi \to 0$ for $\Phi^* \neq \Phi_0$ (contrast this feature with the analysis of §3a). Thus, we have a 5-parameter space in general $(D, T_s, \Phi_0, \Phi^*, \delta\Phi)$, which is difficult to map out in its entirety. Some insight can be obtained from the resulting map of $\overline{\Phi}(1 - D, T_s)$ over the phase space (D, T_s) for different initial hematocrit Φ_0. Figure 6 shows contours of $\overline{\Phi}(1 - D, T_s)$ for three values of the initial hematocrit Φ_0 (0.2, 0.5 and 0.7). Contours are spaced $\delta\Phi = 0.05$ apart. For each panel of figure 6, we note the presence of a roughly triangular region with one side along the $T_s = 0$ axis. Within the tolerance, this region corresponds with the shaded triangular regions in figure 4, where $\Phi(1 - D, T_s)$, and therefore $\overline{\Phi}(1 - D, T_s)$, is identical to the initial value Φ_0. Outside of this region a range of $\overline{\Phi}$ is obtained for different combinations of D and T_s, corresponding to the possibility of achieving different target Φ^*.

As expected, subsampling close to the top of the container ($D \approx 1$) results in a more dilute suspension ($\overline{\Phi} < \Phi_0$), whereas subsampling near the bottom of the container ($D \approx 0$) leads to a more concentrated suspension ($\overline{\Phi} > \Phi_0$). As $T \to \infty$ the system approaches the static solution $\Phi(Z, T) = \Theta[Z - (1 - \Phi_0)]$ as discussed in §2, so that the side channel samples $\overline{\Phi} \sim 0$ if $D > \Phi_0$, and $\overline{\Phi} \sim 1$ if $D < \Phi_0$. For relatively small $\Phi_0 \lesssim 0.5$ (e.g. figure 6a), dilution of the subsample to a prescribed $\Phi^* < \Phi_0$ can be achieved for a larger regions of the (T_s, D) design space, while precise concentration to $\Phi^* > \Phi_0$ restricts solutions to a narrower range of the design space. This behaviour is reversed for a more concentrated initial suspension—it is easier to further
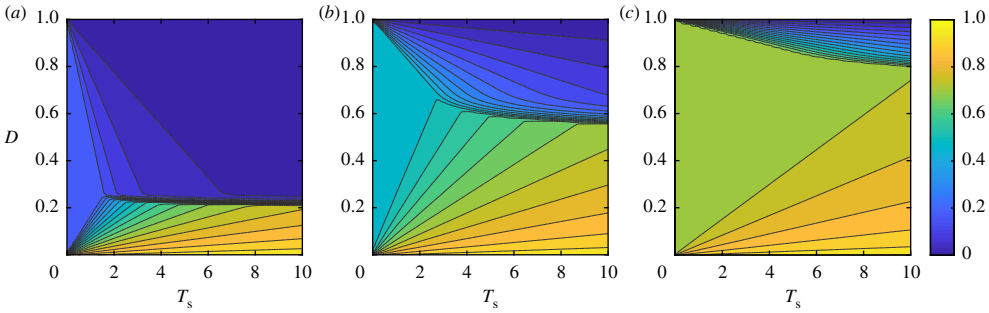
Figure 6. Map of the mean hematocrit $\overline{\Phi}(1 - D, T_s)$ obtained for a given side channel height D and sampling time T_s for different initial hematocrit values Φ_0: (a) 0.2, (b) 0.5 and (c) 0.7. Contours are $\delta\Phi = 0.05$ apart. Colours correspond to $\overline{\Phi}(1 - D, T_s)$, with the scale indicated by the colour bar on the right. The triangular regions attached to the $T_s = 0$ axis are comparable with the shaded regions of figure 4 and correspond to representative subsampling. The remainder of the (D, T_s) space represents either undersampling ($\overline{\Phi} < \Phi_0$) or oversampling ($\overline{\Phi} > \Phi_0$), corresponding to contours terminating at $D = 1$ or $D = 0$, respectively. The sample can be diluted for a larger region of the design space for small Φ_0 (e.g. (a)) whereas the opposite is true for a large Φ_0 (e.g. (c)). (Online version in colour.)

concentrate it (oversample) to a precise value than to dilute it (undersample) with similar precision (e.g. figure 6c). For intermediate values $\Phi_0 \approx 0.5$, both dilution and concentration to a prescribed precision allow similarly sized regions of the design space (e.g. figure 6b). We recall that typically $\Phi_0 \approx 0.6$ for blood, suggesting that using sedimentation it is somewhat easier to concentrate than to dilute a sample with precision.

4. Filling the side channel

The implicit assumption so far is that the suspension drawn into the side channel is well represented by the properties of the suspension in the reservoir at the vertical location $Z = 1 - D$. However, the uptake of fluid into the side channel is itself a dynamic process that depends on several factors including the time-dependent viscosity η of the suspension at the mouth of the side channel (a result of the time-dependent hematocrit $\Phi(Z, T)$), the elapsed time and the mechanism by which fluid is pumped into the side channel.

To illustrate this point, we assume that the fluid is driven into the side channel due to an imposed pressure drop Δp that may be time-dependent. For clarity, we denote the hematocrit in the side channel by $\psi(x, t)$, where $(x = 0, z = h - d)$ represents the mouth of the side channel where it meets the reservoir (figure 1). The side channel is initially devoid of any fluid. Over time, the sample is drawn into the side channel, occupying a length $\ell(t)$ as shown in figure 1. For an incompressible flow, and a side channel with uniform cross-sectional area A_s, $d\ell/dt$ is equal to the mean fluid velocity $\overline{u}$ at any position $x \le \ell(t)$ in the side channel.

We neglect the motion of cells relative to that of the fluid, which may be important in flows of suspensions in narrow channels and may cause particle accumulation [42] or instabilities at the propagating free surface [43]. Instead, we assume that cells are advected passively with the flow, and that the local viscosity of the suspension depends only on the local volume fraction $\psi(x, t)$. Then, Darcy's Law for flow in the channel gives

$$\overline{u}(t) = \frac{d\ell}{dt} = -\frac{\kappa}{\eta(\psi(x, t))} \frac{\partial p}{\partial x}, \tag{4.1}$$

where κ is the permeability of the channel and depends on its cross-sectional shape and $p(x, t)$ is the pressure. The volumetric flux through the side channel is $q = \overline{u}A_s$. Integrating (4.1) yields

$$\Delta p = \frac{1}{\kappa} \frac{d\ell}{dt} \int_0^{\ell} \eta(\psi(x, t)) \, dx. \tag{4.2}$$
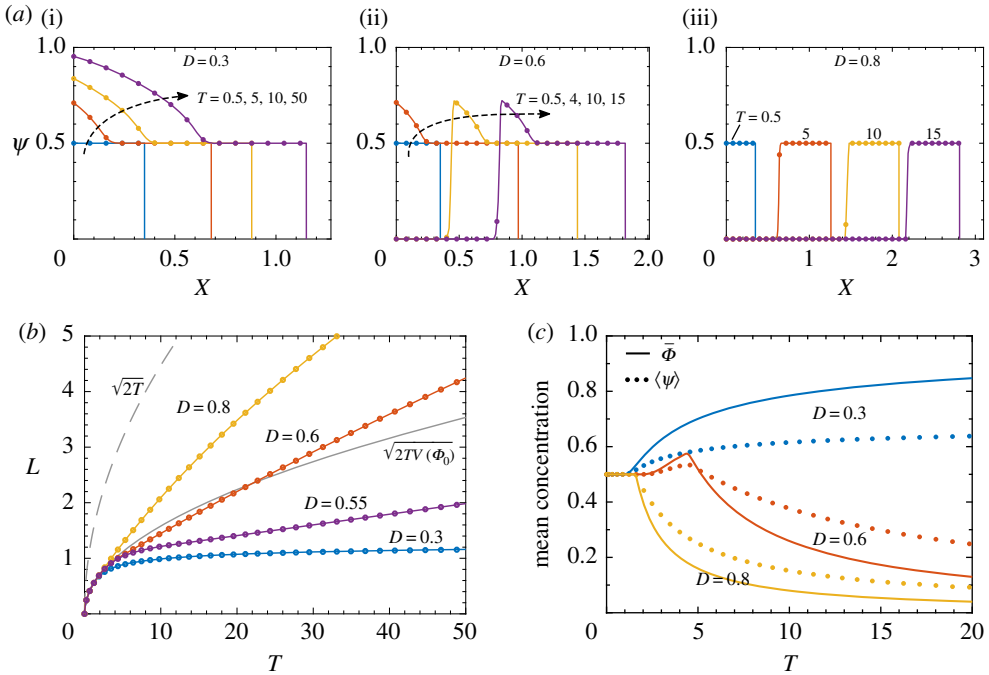
Figure 7. Transport in a side channel at a constant pressure difference across the channel for $\Phi_0 = 0.5$. (a(i)–a(iii)) Profiles of rescaled hematocrit $\Psi(X, T)$ versus X for different times (indicated by dashed arrows or labels) with (a(i)) $D = 0.3$, (a(ii)) $D = 0.6$ and (a(iii)) $D = 0.8$. (b) Filling length in the side channel $L(T)$ for different D, showing that $L(T) \sim \sqrt{2TV(\Phi_0)}$ for short times. (c) Mean concentrations $\overline{\Phi}(1 - D, T)$ (symbols) and $\langle \Psi \rangle (T)$ for a constant pressure drop across the side channel (curves), plotted versus time T, for different channel heights D. Both averages are equal to each other and to Φ_0 for a range of times corresponding to shaded regions in figures 4 and 5 (representative subsampling). Beyond this time $\overline{\Phi} \neq \langle \Psi \rangle \neq \Phi_0$, with $\langle \Psi \rangle$ deviating comparatively less from Φ_0 than $\overline{\Phi}$. (Online version in colour.)

Assuming that cells are passively advected by the mean fluid flow, the transport equation for ψ in the side channel is

$$\frac{\partial \psi}{\partial t} + \frac{\mathrm{d}\ell}{\mathrm{d}t} \frac{\partial \psi}{\partial x} = 0, \tag{4.3}$$

with the initial condition $\psi(x = 0, t) = \phi(z = h - d, t) \equiv \psi_0(t)$. The governing equation is satisfied by a general solution of the form $\psi = f(\ell(t) - x)$, where f is an arbitrary function. Using the initial condition determines f, yielding the solution

$$\psi(x, t) = \psi_0(\ell^{-1}(\ell(t) - x)), \tag{4.4}$$

where ℓ^{-1} is the inverse function defined such that $\ell(t) = x \iff \ell^{-1}(x) = \ell^{-1}(\ell(t)) = t$. Physically, $\ell^{-1}(\ell(t) - x)$ is the time t^* required to fill the side channel up to a length $\ell^* = \ell(t) - x$, i.e. $\ell(t^*) = \ell^*$. Combining (4.4) with (4.2) yields an integro-differential equation for $\ell(t)$,

$$\frac{\mathrm{d}\ell}{\mathrm{d}t} \int_0^\ell \eta[\psi_0(\ell^{-1}(\ell(t) - x))]\, \mathrm{d}x = \kappa\, \Delta p, \tag{4.5}$$

where we note that Δp may be time-dependent.

First, we consider the case of a constant applied Δp. We rescale time as before ($T = tv_0/h$) since the initial condition $\psi_0(t)$ has features set by sedimentation in the reservoir. We use a Krieger–Dougherty viscosity law consistent with (2.1), to write $\eta(\psi) = \eta_0(1 - \psi/\phi_m)^{-k}$, as discussed in §2. Next, we use (4.5) to scale horizontal distances by $\ell_{\Delta p} = \{\kappa h \Delta p/(\eta_0 v_0)\}^{1/2}$ and define $X = x/\ell_{\Delta p}$ and $L(T) = \ell(t)/\ell_{\Delta p}$. Defining $\Psi(X, T) = \psi(x, t)/\phi_m$ so that $\eta(\psi) = \eta_0/V(\Psi)$ [see (2.3)], (4.5) rescales

as

$$\frac{dL}{dT} \int_0^L \frac{dX}{V[\Psi_0(L^{-1}(L(T) - X)))]} = 1, \tag{4.6}$$

where $\Psi_0(T) = \Psi(0, T) = \Phi(1 - D, T)$ and $L^{-1}(L(T)) = T$. Then, the spatially averaged dimensionless hematocrit of the subsample in the side channel is

$$\langle \Psi \rangle (T) = \frac{1}{L(T)} \int_0^{L(T)} \Psi(X, T) \, dX. \tag{4.7}$$

If $\Psi_0(T) = \Psi_0$ is constant over the time of interest, we find

$$L(T) = L_0(T) \equiv (2TV(\Psi_0))^{1/2} \tag{4.8}$$

or $\ell(t) = (2t\kappa \Delta p / \eta(\psi_0))^{1/2}$, which is a result similar to capillary imbibition of wetting fluids. This result corresponds to subsampling within the shaded regions of the design space in figures 4 and 5, for which the hematocrit at the opening of side channel ($z = h - d$, $x = 0$) is equal to that of the original sample (representative subsampling). Consequently, the subsample in the side channel is spatially homogeneous and is representative of the original sample in terms of hematocrit, i.e. $\Psi(X, T) = \langle \Psi \rangle (T) = \Phi(1 - D, T) = \Phi_0$.

Outside of these solution regions, the subsample becomes spatially inhomogeneous since the conditions presented to the inlet of the side channel change over time. We solve (4.6) numerically by first-order Euler integration, using $L(T) \sim L_0(T) = (2TV(\Psi_0))^{1/2}$ as an asymptotic result as $T \to 0$. Figure 7a(i)–a(iii) shows profiles of Ψ versus X at different times and for different sampling heights. For $D < \Phi_0$ (figure 7a(i)), the concentration at the mouth of the side channel increases in time due to sedimentation in the reservoir. The opposite is true for $D > \Phi_0$ (figure 7a(ii)–a(iii)) where the side channel eventually samples $\Phi = 0$ fluid. For some values of $D \gtrsim \Phi_0$, the inlet concentration first increases and then decreases to zero at the inlet $X = 0$, leading to a non-trivial distribution $\Psi(X, T)$ in the side channel (figure 7a(ii)).

The growth of $L(T)$ is plotted in figure 7b for different values of D. In all cases $L \sim L_0(T)$ initially, with late time dynamics depending on the location D of the side port. We recall the steady-state sedimentation solution $\Phi(Z, T \to \infty) \to \Theta[Z - (1 - \Phi_0)]$. Thus, for $D < \Phi_0$, the side channel samples increasingly more concentrated suspension, resulting in $L(T)$ approaching a constant value. For any $D > \Phi_0$, $L(T)$ grows indefinitely and may either be faster or slower than $L_0(T)$ at any finite time T, though it is guaranteed to be asymptotically faster than this early-time growth law as $T \to \infty$ since the side channel takes up only (low viscosity) plasma beyond a certain time.

It is reasonable to expect the mean hematocrit of the subsample $\langle \Psi \rangle$ to be close to $\overline{\Phi}$, as discussed earlier. However, there are two sources of systematic deviation from this value. First, the flux into the side channel is greater for lower hematocrit (due to lower viscosity) resulting in a bias towards lower average cell concentrations over the entire side channel. Second, the flux is greater at earlier times when $\ell(t)$ is small (due to greater $|\partial p / \partial x| = \Delta p / \ell(t)$), so the mean subsample hematocrit is biased towards earlier parts of the inlet condition $\phi_0(t)$. The spatially averaged subsample hematocrit $\langle \Psi \rangle$ is plotted in figure 7c for different D, showing the time average at the mouth of the side channel, $\overline{\Phi}(1 - D, T)$, for comparison. As expected, the two averages are identical to each other and to Φ_0 for sufficiently short times (representative sampling). At a critical time that depends on D (figure 4) both quantities deviate from Φ_0 and from each other. For the reasons discussed above, we observe a tendency for $\langle \Psi \rangle$ to remain closer to the initial value Φ_0 than $\overline{\Phi}$. We also note that the deviations between $\langle \Psi \rangle$ and $\overline{\Phi}$ are larger for $\overline{\Phi} > \Phi_0$, consistent with the argument that high-concentration fluid has a greater resistance to flow and therefore less of it is drawn into the channel.

Finally, we note that in practice the pressure may be modulated so that the suspension is drawn into the side channel at constant volumetric flux (e.g. using a syringe pump). We retain rescaled variables as before, with the caveat that lengths are rescaled by a reference length $\ell_q = qh/v_0 A_s$ instead of $\ell_{\Delta p}$. At constant flux through a channel with constant cross-sectional area, dL/dT is constant, so that (4.3) admits the solution $\Psi(X, T) = \Psi_0(T(1 - X/L))$. Consequently, the space-averaged hematocrit in the side channel is equal to the time-averaged hematocrit at its inlet,

i.e. $\langle \Psi \rangle (T)|_{q=\text{const.}} = \overline{\Phi}(1 - D, T)$. This result for constant-flux pumping into the side channel is in contrast with the case of constant-pressure pumping, as discussed above and plotted in figure 7c.

Thus, the transport of the suspension within the channel adds an additional layer of complexity to sampling, over features arising from sedimentation in the reservoir, particularly when this transport is pressure-controlled. We note that the presence of viscosity gradients in the channel may produce additional flow features such as instabilities. Furthermore, interactions of cells with channel walls or with the fluid velocity distribution may cause the cells to either lag or accumulate near the moving front in the side channel. These effects are beyond the focus of this study but may be important in applications.

5. Concluding remarks

We have developed design considerations to optimize the problem of subsampling suspensions settling in a reservoir, with a particular focus on blood, which may be relevant to some classes of diagnostic devices. Using an experimentally guided Krieger–Dougherty Law along with a one-dimensional Kynch sedimention model, we identify combinations of design parameters that ensure representative subsampling; these parameters relate to (i) the geometry of the container holding the original suspension, and (ii) the location of the side channel where subsampling occurs. Furthermore, we explore the possibility of extracting a subsample that is either more or less concentrated than the original sample. We find that doing so with precision depends on several factors including the process by which fluid is pumped into the side channel in which the subsample is collected. We find important distinctions between flux-controlled and pressure-controlled pumping into the side channel, particularly outside the solution region for representative sampling.

In the present work, it is implicit that the suspension may be treated as a continuum both in the reservoir and the subsampling channel. This assumption may need to be modified particularly if the side channel has transverse dimensions comparable with that of a single cell. Furthermore, at such scales, the deformability of erythrocytes becomes an important feature. Flowing suspensions in narrow channels may also result in further particle separation or instabilities that are not modelled here. Nonetheless, our present work provides systematic guiding principles to design devices that extract subsamples from a larger volume of a suspension, such as blood, in ways that either exploit or compensate for sedimentation.

References

1. Cui F, Rhee M, Singh A, Tripathi A. 2015 Microfluidic sample preparation for medical diagnostics. *Annu. Rev. Biomed. Eng.* **17**, 267–286. (doi:10.1146/annurev-bioeng-071114-040538)
2. Kersaudy-Kerhoas M, Sollier E. 2013 Micro-scale blood plasma separation: from acoustophoresis to egg-beaters. *Lab Chip* **13**, 3323–3346. (doi:10.1039/c3lc50432h)
3. Homsy A *et al.* 2012 Development and validation of a low cost blood filtration element separating plasma from undiluted whole blood. *Biomicrofluidics* **6**, 012804. (doi:10.1063/1.3672188)
4. Lu Z, Rey E, Vemulapati S, Srinivasan B, Mehta S, Erickson D. 2018 High-yield paper-based quantitative blood separation system. *Lab Chip* **18**, 3865–3871. (doi:10.1039/C8LC00717A)
5. Faivre M, Abkarian M, Bickraj K, Stone HA. 2006 Geometrical focusing of cells in a microfluidic device: an approach to separate blood plasma. *Biorheology* **43**, 147–159.

6. Wu CC, Hong LZ, Ou CT. 2012 Blood cell-free plasma separated from blood samples with a cascading Weir-type microfilter using dead-end filtration. *J. Med. Biol. Eng.* **32**, 163–168. (doi:10.5405/jmbe.937)

7. Kuo JN, Lin BY. 2018 Microfluidic blood-plasma separation chip using channel size filtration effect. *Microsys. Tech.* **24**, 2063–2070. (doi:10.1007/s00542-017-3607-2)

8. Minerick AR, Ostafin AE, Chang HC. 2002 Electrokinetic transport of red blood cells in microcapillaries. *Electrophoresis* **23**, 2165–2173. (doi:10.1002/1522-2683(200207)23:14<2165::AID-ELPS2165>3.0.CO;2-#)

9. Jung J, Han KH. 2008 Lateral-driven continuous magnetophoretic separation of blood cells. *Appl. Phys. Lett.* **93**, 223902. (doi:10.1063/1.3036898)

10. Kim J, Massoudi M, Antaki JF, Gandini A. 2012 Removal of malaria-infected red blood cells using magnetic cell separators: a computational study. *Appl. Math. Comp.* **218**, 6841–6850. (doi:10.1016/j.amc.2011.12.057)

11. Tasoglu S, Khoory JA, Tekin HC, Thomas C, Karnoub AE, Ghiran IC, Demirci U. 2015 Levitational image cytometry with temporal resolution. *Adv. Mater.* **27**, 3901–3908. (doi:10.1002/adma.201405660)

12. Lenshof A, Ahmad-Tajudin A, Järås K, Swärd-Nilsson AM, Åberg L, Marko-Varga G, Malm J, Lilja H, Laurell T. 2009 Acoustic whole blood plasmapheresis chip for prostate specific antigen microarray diagnostics. *Anal. Chem.* **81**, 6030–6037. (doi:10.1021/ac9013572)

13. Mach AJ, Di Carlo D. 2010 Continuous scalable blood filtration device using inertial microfluidics. *Biotech. Bioeng.* **107**, 302–311. (doi:10.1002/bit.22833)

14. Dimov IK, Basabe-Desmonts L, Garcia-Cordero JL, Ross BM, Ricco AJ, Lee LP. 2011 Stand-alone self-powered integrated microfluidic blood analysis system (SIMBAS). *Lab Chip* **11**, 845–850. (doi:10.1039/C0LC00403K)

15. Maria MS, Rakesh PE, Chandra TS, Sen AK. 2017 Capillary flow-driven microfluidic device with wettability gradient and sedimentation effects for blood plasma separation. *Sci. Rep.* **7**, 43457. (doi:10.1038/srep43457)

16. Zhang XB, Wu ZQ, Wang K, Zhu J, Xu JJ, Xia XH, Chen HY. 2012 Gravitational sedimentation induced blood delamination for continuous plasma separation on a microfluidics chip. *Anal. Chem.* **84**, 3780–3786. (doi:10.1021/ac3003616)

17. Li T, Zhang L, Leung KM, Yang J. 2010 Out-of-plane microvalves for whole blood separation on lab-on-a-CD. *J. Micromech. Microeng.* **20**, 105024. (doi:10.1088/0960-1317/20/10/105024)

18. Zhang J, Guo Q, Liu M, Yang J. 2008 A lab-on-CD prototype for high-speed blood separation. *J. Micromech. Microeng.* **18**, 125025. (doi:10.1088/0960-1317/18/12/125025)

19. Freund JB. 2014 Numerical simulation of flowing blood cells. *Annu. Rev. Fluid Mech.* **46**, 67–95. (doi:10.1146/annurev-fluid-010313-141349)

20. Tomaiuolo G. 2014 Biomechanical properties of red blood cells in health and disease towards microfluidics. *Biomicrofluidics* **8**, 051501. (doi:10.1063/1.4895755)

21. Forsyth AM, Wan J, Owrutsky PD, Abkarian M, Stone HA. 2011 Multiscale approach to link red blood cell dynamics, shear viscosity, and ATP release. *Proc. Natl Acad. Sci. USA* **108**, 10 986–10 991. (doi:10.1073/pnas.1101315108)

22. Lanotte L, Mauer J, Mendez S, Fedosov DA, Fromental JM, Claveria V, Nicoud F, Gompper G, Abkarian M. 2016 Red cells' dynamic morphologies govern blood shear thinning under microcirculatory flow conditions. *Proc. Natl Acad. Sci. USA* **113**, 13 289–13 294. (doi:10.1073/pnas.1608074113)

23. Secomb TW. 2017 Blood flow in the microcirculation. *Annu. Rev. Fluid Mech.* **49**, 443–461. (doi:10.1146/annurev-fluid-010816-060302)

24. Guo Q, Duffy SP, Matthews K, Santoso AT, Scott MD, Ma H. 2014 Microfluidic analysis of red blood cell deformability. *J. Biomech.* **47**, 1767–1776. (doi:10.1016/j.jbiomech.2014.03.038)

25. Pivkin IV, Peng Z, Karniadakis GE, Buffet PA, Dao M, Suresh S. 2016 Biomechanics of red blood cells in human spleen and consequences for physiology and disease. *Proc. Natl Acad. Sci. USA* **113**, 7804–7809. (doi:10.1073/pnas.1606751113)

26. Miller A, Green M, Robinson D. 1983 Simple rule for calculating normal erythrocyte sedimentation rate. *Brit. Med. J.* **286**, 266. (doi:10.1136/bmj.286.6361.266)

27. Jacobson DM, Slamovits TL. 1987 Erythrocyte sedimentation rate and its relationship to hematocrit in giant cell arteritis. *Arch. Ophthalmol.* **105**, 965–967. (doi:10.1001/archopht.1987.01060070101037)

28. Sun M, Khan ZS, Vanapalli SA. 2012 Blood plasma separation in a long two-phase plug flowing through disposable tubing. *Lab Chip* **12**, 5225–5230. (doi:10.1039/c2lc40544j)

29. Brigden ML. 1999 Clinical utility of the erythrocyte sedimentation rate. *Am. Fam. Physician* **60**, 1443–1450.

30. Rourke MD, Ernstene AC. 1930 A method for correcting the erythrocyte sedimentation rate for variations in the cell volume percentage of blood. *J. Clin. Invest.* **8**, 545–559. (doi:10.1172/JCI100278)

31. Ropes MW, Rossmeisl E, Bauer W. 1939 The relationship between the erythrocyte sedimentation rate and the plasma proteins. *J. Clin. Invest.* **18**, 791–798. (doi:10.1172/JCI101096)

32. Fabry TL. 1987 Mechanism of erythrocyte aggregation and sedimentation. *Blood* **70**, 1572–1576.

33. Schneider CA, Rasband WS, Eliceiri KW. 2012 NIH Image to ImageJ: 25 years of image analysis. *Nature Meth.* **9**, 671–675. (doi:10.1038/nmeth.2089)

34. Krieger IM, Dougherty TJ. 1959 A mechanism for non-Newtonian flow in suspensions of rigid spheres. *Trans. Soc. Rheol.* **3**, 137–152. (doi:10.1122/1.548848)

35. Horner JS, Armstrong MJ, Wagner NJ, Beris AN. 2018 Investigation of blood rheology under steady and unidirectional large amplitude oscillatory shear. *J. Rheol.* **62**, 577–591. (doi:10.1122/1.5017623)

36. Apostolidis AJ, Beris AN. 2014 Modeling of the blood rheology in steady-state shear flows. *J. Rheol.* **58**, 607–633. (doi:10.1122/1.4866296)

37. Tomaiuolo G, Carciati A, Caserta S, Guido S. 2016 Blood linear viscoelasticity by small amplitude oscillatory flow. *Rheol. Acta* **55**, 485–495. (doi:10.1007/s00397-015-0894-3)

38. Kynch GJ. 1952 A theory of sedimentation. *Trans. Faraday Soc.* **48**, 166–176. (doi:10.1039/tf9524800166)

39. Bustos MC, Tory EM, Bürger R, Concha F. 1999 *Sedimentation and thickening: phenomenological foundation and mathematical theory*, vol. 8. Dordrecht, The Netherlands: Kluwer Academic Publishers.

40. Whitham GB. 1974 *Linear and nonlinear waves*. New York, NY: John Wiley & Sons.

41. Harten A, Lax PD, Leer Bv. 1983 On upstream differencing and Godunov-type schemes for hyperbolic conservation laws. *SIAM Rev.* **25**, 35–61. (doi:10.1137/1025002)

42. Holloway W, Aristoff JM, Stone HA. 2011 Imbibition of concentrated suspensions in capillaries. *Phys. Fluids* **23**, 081701. (doi:10.1063/1.3619217)

43. Kim J, Xu F, Lee S. 2017 Formation and destabilization of the particle band on the fluid-fluid interface. *Phys. Rev. Lett.* **118**, 074501. (doi:10.1103/PhysRevLett.118.074501)